 CMES, vol.107, no.3, pp.249-276, 2015

Structural-Acoustic Design Sensitivity Analysis based on Direct Differentiation Method with Different Element Types

L.L. Chen[1] **and H.B. Chen**[1,2]

Abstract: Engineers have started to develop ways to decrease noise radiation. Structural-acoustic design sensitivity analysis can provide information on how changes in design variable affect the radiated acoustic performance. As such, it is an important step in the structural-acoustic design and in optimization processes. For thin structures immersed in water, a full interaction between the structural domain and the fluid domain needs to be taken into account. In this work, the finite element method is used to model the structure parts and the boundary element method is applied to the exterior acoustic problem. The formula of the sound pressure sensitivity based on the direct differentiation method is presented. The design variable can be chosen as the material parameters, structure and fluid parameters, such as the fluid density, structural density, Poisson's ratio, Young's modulus, structural shape size and so on. Numerical examples are presented to demonstrate the validity of the proposed algorithm. Different types elements are used for the numerical solution, and the performance of different types of FE/BE element is presented and compared.

Keywords: Fluid-structure interaction, FE/BE coupling, Design sensitivity analysis, Discontinuous element, Direct differentiation method.

1 Introduction

Acoustic design sensitivity analysis can provide information on how changes in geometry affect the acoustic performance of a given structure. As such, it is an important step in the acoustic design and in optimization processes. An overview of the developments in structural-acoustic optimization for passive noise control

[1] Department of Modern Mechanics, University of Science and Technology of China, CAS Key Labaratory of Mechanical Behavior and Design of Materials, Hefei 230027, Anhui, P.R.China.

[2] Corresponding Author. Phone:+86-0551-63600345. Fax:+86-0551-63606459. Email: hbchen@ustc.edu.cn

was presented in [Marburg (2002)]. The global finite difference method is widely applied to structural-acoustic optimization because it is easy to implement [Lamancusa (1993); Hambric (1996)]. However, this method performs inefficiently especially when many design variables are taken into account concurrently. Analytic and semi-analytic sensitivity analyses are much more accurate and require less computational costs than the global finite difference method. Analytic sensitivity analysis, which appeared as the direct differentiation method, was applied to structural acoustic problems in [Chen, Zheng, and Chen (2013); Chen, Chen, and Zheng (2013); Chen, Zheng, and Chen (2014); Zheng, Matsumoto, Takahashi, and Chen (2012); Fritze, Marburg, and Hardtke (2005)]. Another method, which appeared as the adjoint variable method [Choi, Shim, and Wang (1997); Wang (1999); Matsumoto, Yamada, Takahashi, Zheng, and Harada (2011); Zheng, Chen, Matsumoto, and Takahashi (2011)], is very useful for sensitivity analysis with many design variables. In the present paper, the direct differentiation method is applied for sensitivity analysis.

The finite element method (FEM) was used to model the structure parts of a problem because of its high flexibility and applicability to large-scale practical models. The boundary element method (BEM) can also be used to model the structure parts [Qian, Batra, and Chen (2003); Han and Atluri (2002); Okada, Fukui, and Kumazawa (2004)], and it is a better method to model the exterior sound field to avoid the need to mesh the fluid domain [Qian, Han, and Atluri (2013); Qian, Han, Ufimtsev, and Atluri (2004); Qian, Han, and Atluri (2004);Chien, Rajiyah, and Atluri (1990)]. As such a suitable approach for the analysis of fluid-structure interaction problems is the coupling FE/BE method [Lie, Yu, and Zhao (2001); Everstine and Henderson (1990); Merz, Kinns, and Kessissoglou (2009); Chen, Hofstetter, and Mang (1998); Schneider (2008); Brunner, Junge, and Gaul (2009); Fischer and Gaul (2005); Junge, Brunner, and Gaul (2011); Peters, Marburg, and Kessissoglou (2012)]. For the FE/BE algorithm, non-conforming discretizations at interaction surface allow an independent mesh shape and size for the fluid and structure domain. Many approaches have been developed to generate the non-conforming meshes, such as the Mortar method [Peters, Marburg, and Kessissoglou (2012)], in which the coupling conditions at the common interface are formulated in a weak sense. Results with higher accuracy can be obtained using non-conforming discretizations. However, for simplicity, the identical mesh for structure and fluid at the interface is used for the numerical solution in this paper.

For BEM, the approach of continuous linear and quadratic elements is often applied, and the alternative of discontinuous elements with higher accuracy was investigated in [Rego-Silva (1993); Tadeu and Antonio (2000); Marburg and Schneider (2003)]. The effect of superconvergence for error dependence upon element

size for discontinuous boundary elements when collocation points are located at the zeros of orthogonal functions for the standard interval was reviewed in [Atkinson (1997)]. Error dependence in terms of frequency, element size, and location of nodes on discontinuous elements is presented in [Marburg and Schneider (2003)], and the result that discontinuous boundary elements perform more efficiently than continuous ones is also obtained in [Marburg and Schneider (2003)]. The performance of the discontinuous boundary element for the rigid analysis in structural-acoustic domain has also been thoroughly investigated. However, few papers described the performance of the discontinuous boundary element coupled by FEM when the interaction between the structure and fluid is taken into account.

The constant boundary element coupled by finite element is widely used to the numerical solution for practical problems [Brunner, Junge, and Gaul (2009); Junge, Brunner, and Gaul (2011); Merz, Kinns, and Kessissoglou (2009); Everstine and Henderson (1990)], where the FE/BE element with linear shape function leads to lines in 2D or triangles and quadrilaterals in 3D. The FE/BE element with quadratic shape functions is used for the structural-acoustic analysis in [Peters, Marburg, and Kessissoglou (2012)], but not for the structural-acoustic sensitivity analysis. In this paper, different types of FE/BE element are used for sensitivity analysis, and their performance are compared in detail. The disadvantage of the linear shape functions is that a curved surface is not well-represented, which causes gaps, overlaps, and angles between elements of both meshes in the normal direction of the interaction surface. As such, the more error arises when calculating the integration on the boundary surface. Moreover, the coordinate of interpolation node obtained using linear shape approximation deviates from the analytical nodal coordinate for a curved surface, and more errors are produced. A possible solution to avoid these disadvantages is the use of quadratic shape functions. Although it does not provide the perfect fit for curved interfaces, the gaps and overlaps in the normal direction of the interface are significantly reduced.

This paper presents the formula of the sound pressure sensitivity with respect to the design variables, where the design variable can be chosen as the fluid density, structural density, Poisson's ratio, Young's modulus, structural shape size, and so on. Two numerical examples are presented to demonstrate the validity and correctness of the present algorithm. In this paper, several types coupling schemes are used for the numerical solution, and the performance of different types of FE/BE coupling schemes is presented and compared. The discontinuous linear boundary elements with quadratic shape approximation was found to perform more efficiently than the constant boundary elements with linear shape approximation by observing the result for the surface error.

2 Structural-acoustic formulation

For the fluid, the discretization of the Helmholtz integral equation obtained using BEM results in a system of equations that can be written as

$$\mathbf{Hp} = \mathbf{Gq} + \mathbf{p_i}, \tag{1}$$

where $\mathbf{G}$ and $\mathbf{H}$ are the influence matrices, $\mathbf{p}$ and $\mathbf{q}$ are the column matrices that contain the nodal boundary values of the sound pressure and their normal derivatives, and $\mathbf{p_i}$ contains the nodal values of the incident pressure field.

FEM for structures have been thoroughly described and discussed in many papers. In general, these methods result in a system of equations [Fritze, Marburg, and Hardtke (2005)]

$$\mathbf{Au} = \mathbf{f}, \tag{2}$$

where $\mathbf{A} = \mathbf{K} + i\omega\mathbf{C} - \omega^2\mathbf{M}$, $i = \sqrt{-1}$, $\mathbf{M}$ the mass matrix, $\mathbf{K}$ the stiffness matrix, $\mathbf{C}$ the damping matrix, and $\mathbf{u}$ the nodal displacement vector. Taking into account the effect of the acoustic pressure at the structural surfaces, we applied an acoustic load $\mathbf{C_{sf}p}$ along with the structural load $\mathbf{f_s}$, and the excitation can be expressed as:

$$\mathbf{f} = \mathbf{f_s} + \mathbf{C_{sf}p}, \tag{3}$$

where the coupling matrix $\mathbf{C_{sf}}$ can be expressed as [Fritze, Marburg, and Hardtke (2005)]:

$$\mathbf{C_{sf}} = \int_{\Gamma_{int}} \mathbf{N_s^T n N_f} d\Gamma_{int}, \tag{4}$$

where Γ_{int} denotes the interaction surface, $\mathbf{N_s}$ and $\mathbf{N_f}$ are the global interpolation functions for the structure and fluid domains, respectively, and $\mathbf{n}$ is the surface normal vector. By substituting Eq. (3) into Eq. (2), we can obtain the following formula

$$\mathbf{u} = \mathbf{A}^{-1}\mathbf{f_s} + \mathbf{A}^{-1}\mathbf{C_{sf}p}. \tag{5}$$

After having presented the systems of equations for the fluid and for the structure separately, the coupling condition needs to be formulated, as follows

$$\mathbf{q} = \omega^2\rho\mathbf{S}^{-1}\mathbf{C_{fs}u}, \tag{6}$$

where $\mathbf{C_{fs}} = \mathbf{C_{sf}^T}$ and $\mathbf{S} = \int_{\Gamma_{int}} \mathbf{N_f^T N_f} d\Gamma_{int}$.

In the next step, the coupling condition is applied to Eq. (1) to substitute for $\mathbf{q}$. This process yields

$$\mathbf{Hp} = \omega^2 \rho \mathbf{G} \mathbf{S}^{-1} \mathbf{C_{fs}} \mathbf{u} + \mathbf{p_i}. \tag{7}$$

Eq. (2) and Eq. (7) can be combined to a coupled system of equations, as follows

$$\begin{bmatrix} \mathbf{A} & -\mathbf{C_{sf}} \\ -\omega^2 \rho \mathbf{G} \mathbf{S}^{-1} \mathbf{C_{fs}} & \mathbf{H} \end{bmatrix} \begin{Bmatrix} \mathbf{u} \\ \mathbf{p} \end{Bmatrix} = B \begin{Bmatrix} \mathbf{u} \\ \mathbf{p} \end{Bmatrix} = \begin{Bmatrix} \mathbf{f_s} \\ \mathbf{p_i} \end{Bmatrix}. \tag{8}$$

In fact, direct iterations on the combined equation shown above converge very slowly, and solving the system equation directly will take much more computing time and storage requirement. In addition, obtaining the numerical solutions with high accuracy is difficult. Instead of solving the above non-symmetric system of linear equation by using an iterative solver, we propose the following approach. By substituting Eq. (5) into Eq. (7), the following coupled boundary element equation can be obtained [Fritze, Marburg, and Hardtke (2005)]

$$\mathbf{Hp} - \mathbf{GWC_{sf}p} = \mathbf{GWf_s} + \mathbf{p_i}, \tag{9}$$

where $\mathbf{W} = \omega^2 \rho \mathbf{S}^{-1} \mathbf{C_{fs}} \mathbf{A}^{-1}$. The term $\mathbf{A}^{-1}\mathbf{f_s}$ in the right side of Eq. (9) represents solution $\mathbf{x}$ of the linear system of equations $\mathbf{Ax} = \mathbf{f_s}$. This symmetric and frequency-dependent system is easily solved using a sparse direct solver. Directly solving the term $\mathbf{A}^{-1}\mathbf{C_{sf}}$ in the left side of Eq. (9) is unnecessary. In this study, the iterative solver generalized minimal residual method (GMRES) [Saad (1996)] is applied to accelerate the calculation of the solution to the coupled boundary element system equation. The current iterative solution is assumed as $\mathbf{p_k}$. First, the matrix-vector product of $\mathbf{C_{sf}p_k}$ and a new vector $\mathbf{y}$ is calculated, where $\mathbf{y} = \mathbf{C_{sf}p_k}$. The solution of $\mathbf{A}^{-1}\mathbf{y}$ can then be obtained efficiently when a sparse direct solver is used to solve the symmetric and frequency-dependent system of linear equation $\mathbf{Ax} = \mathbf{y}$. The implementation of a single Helmholtz boundary integral equation in Eq. (9) may have the difficulty of non-uniqueness for exterior boundary-value problems. In this study, the Burton-Miller method is applied to overcome the non-uniqueness problem efficiently [Burton and Miller (1971)]. The strongly singular and hypersingular integrals in the equations can be evaluated explicitly and directly by using the Cauchy principal value and the Hadamard finite part integral method. After solving Eq. (9), the sound pressure values vector $\mathbf{p}$ can be obtained, and the solution of the vector $\mathbf{p}$ can be substituted into Eq. (5). The unknown vector $\mathbf{u}$ can be solved using Eq. (5).

3 Design sensitivity analysis

The structural-acoustic optimization shows high potential in minimizing of radiated noise especially for thin shell geometries. For the optimization process, the

use of design sensitivity, which represents the rate of change of the object function with respect to the design variable, is often desirable. When the sensitivities are obtained, an improved design can be obtained after the iterative calculations. Accordingly, acoustic shape sensitivity analysis is typically the first and most important step in acoustic shape design and optimization processes [Chen, Chen, and Zheng (2013); Zheng, Matsumoto, Takahashi, and Chen (2012)].

The implicit differentiation of Eq. (8) with respect to the design variable ϑ and isolating the resulting sensitivities of structural displacement and sound pressure lead to

$$\mathbf{B}\begin{Bmatrix}\dot{\mathbf{u}}\\ \dot{\mathbf{p}}\end{Bmatrix} = \begin{Bmatrix}\mathbf{r_1}\\ \mathbf{r_2}\end{Bmatrix} = \mathbf{r}, \tag{10}$$

where

$$\mathbf{r} = \begin{Bmatrix}\dot{\mathbf{f}}_\mathbf{s}\\ \dot{\mathbf{p}}_\mathbf{i}\end{Bmatrix} - \dot{\mathbf{B}}\begin{Bmatrix}\mathbf{u}\\ \mathbf{p}\end{Bmatrix}. \tag{11}$$

For different design variables, different expressions of $\dot{\mathbf{B}}$ are obtained. When the fluid density ρ is chosen as the design variable, $\dot{\mathbf{B}}$ is derived by

$$\dot{\mathbf{B}} = \begin{bmatrix}\mathbf{0} & \mathbf{0}\\ -\omega^2\mathbf{G}\mathbf{S}^{-1}\mathbf{C}_\mathbf{fs} & \mathbf{0}\end{bmatrix} \tag{12}$$

and the vector $\mathbf{r}$ is derived by

$$\mathbf{r} = \begin{Bmatrix}\mathbf{r_1}\\ \mathbf{r_2}\end{Bmatrix} = \begin{Bmatrix}\mathbf{0}\\ \omega^2\mathbf{G}\mathbf{S}^{-1}\mathbf{C}_\mathbf{fs}\mathbf{u}\end{Bmatrix}. \tag{13}$$

When the structural parameter is chosen as the design variable, such as structural density ρ_s, Poisson's ratio v, Young's modulus E and thickness of spherical shell h presented in the following numerical example, $\dot{B}$ is derived by

$$\dot{\mathbf{B}} = \begin{bmatrix}\dot{\mathbf{A}} & \mathbf{0}\\ \mathbf{0} & \mathbf{0}\end{bmatrix} \tag{14}$$

and the vector $\mathbf{r}$ is derived by

$$\mathbf{r} = \begin{Bmatrix}\mathbf{r_1}\\ \mathbf{r_2}\end{Bmatrix} = \begin{Bmatrix}-\dot{\mathbf{A}}\mathbf{u}\\ \mathbf{0}\end{Bmatrix}. \tag{15}$$

When the parameter determining the structural nodal coordinate is set as the design variable, such as the radius of spherical shell r presented in the following numerical example, $\dot{\mathbf{B}}$ is derived by

$$\dot{\mathbf{B}} = \begin{bmatrix} \dot{\mathbf{A}} & -\dot{\mathbf{C}}_{\mathbf{sf}} \\ -\omega^2\rho(\dot{\mathbf{GS^{-1}}}\mathbf{C_{fs}}) & \dot{\mathbf{H}} \end{bmatrix} \tag{16}$$

where the upper dot $\dot{(\,)}$ denotes the differentiation with respect to the design variable. The vector $\mathbf{r}$ is derived by

$$\mathbf{r} = \begin{Bmatrix} \mathbf{r_1} \\ \mathbf{r_2} \end{Bmatrix} = \begin{Bmatrix} \dot{\mathbf{f}}_\mathbf{s} - \dot{\mathbf{A}}\mathbf{u} + \dot{\mathbf{C}}_{\mathbf{sf}}\mathbf{p} \\ \dot{\mathbf{p}}_\mathbf{i} + \omega^2\rho(\dot{\mathbf{GS^{-1}}}\mathbf{C_{fs}})\mathbf{u} - \dot{\mathbf{H}}\mathbf{p} \end{Bmatrix}. \tag{17}$$

The expressions of matrices $\dot{\mathbf{A}}$, $\dot{\mathbf{C}}_{\mathbf{sf}}$, $\dot{\mathbf{C}}_{\mathbf{fs}}$, $\dot{\mathbf{S}}^{-\mathbf{1}}$, $\dot{\mathbf{H}}$, and $\dot{\mathbf{G}}$ can be complicated, particularly when the structure domain is approximated using shell finite elements. Hence, solving them directly is difficult. However, the semi-analytical derivative method, through which variations of the coefficient matrices can be calculated using the finite difference method, can be applied to overcome this difficulty. For example, matrix $\dot{\mathbf{C}}$ can be calculated using a small perturbation τ when the shape design variable is denoted by α, as follows:

$$\dot{\mathbf{C}} = \frac{\mathbf{C}(\alpha+\tau) - \mathbf{C}(\alpha)}{\tau}. \tag{18}$$

In this work, a step size $\tau/\alpha = 10^{-3}$ is used. Smaller step size will produce better solution. However, very smaller step size such as 10^{-7} will not produce correct solution, because the data of the structural matrix from ANSYS is single precision. On the other hand, the solution for the step sizes of 10^{-3}, 10^{-4}, 10^{-5} is compared, and found to be very similar. So, step size of 10^{-3} is suitable. Directly solving Eq. (10) is likely to be very inefficient because the system matrix will be quite large for realistic problems. Decomposing the system equation Eq. (10) into two equations, as follows

$$\mathbf{A}\dot{\mathbf{u}} - \mathbf{C}_{\mathbf{sf}}\dot{\mathbf{p}} = \mathbf{r_1} \tag{19}$$

and

$$\mathbf{H}\dot{\mathbf{p}} - \omega^2\rho\mathbf{G}\dot{\mathbf{S^{-1}}}\mathbf{C_{fs}}\dot{\mathbf{u}} = \mathbf{r_2}. \tag{20}$$

By substituting Eq. (19) into Eq. (20), the following formula is obtained

$$\mathbf{H}\dot{\mathbf{p}} - \mathbf{G}\mathbf{W}\mathbf{C}_{\mathbf{sf}}\dot{\mathbf{p}} = \mathbf{G}\mathbf{W}\mathbf{r_1} + \mathbf{r_2}. \tag{21}$$

Equation (21) is very similar to Eq. (9); thus, the same solving method is implemented. By solving the above equation, the sensitivity of the nodal sound pressure on the surface can be obtained. The unknown vector $\dot{\mathbf{u}}$ can be solved by substituting the solution of the vector $\dot{\mathbf{p}}$ into Eq. (19) and solving Eq. (19).

In the following work, we will derive the formulas of the sound pressure sensitivity at the field point in the fluid domain. The boundary integral equation defined on the structure boundary Γ to evaluate the sound pressure at a field point $p(y)$ in the fluid domain can be expressed as

$$p(y) + \int_{\Gamma} F(x,y)p(x)\,\mathrm{d}\Gamma(x) = \int_{\Gamma} G(x,y)q(x)\,\mathrm{d}\Gamma(x), \tag{22}$$

where $q(x)$ and $F(x,y)$ are the normal derivatives of $p(x)$ and $G(x,y)$, respectively; y is the field point; and $G(x,y)$ is the Green's function. For 3D acoustic wave problems, $G(x,y) = \frac{e^{ikr}}{4\pi r}$, where $r = |y-x|$. Discretization of the above formula allows us to evaluate $p(y)$ as

$$p(y) = \mathbf{g}^T(y)\mathbf{q} - \mathbf{h}^T(y)\mathbf{p}, \tag{23}$$

where $\mathbf{g}(y)$ and $\mathbf{h}(y)$ are coefficient vectors. By substituting the vectors $\mathbf{p}$ and $\mathbf{q}$ obtained by solving the coupled boundary element equation (9) into Eq. (23), the value of $p(y)$ can be solved.

When the parameter, such as the fluid density ρ, structural density ρ_s, Poisson's ratio v, Young's modulus E, or the thickness of the spherical shell h presented in the following numerical example, is set as the design variable, we can obtain the following formula by differentiating Eq. (22)

$$\dot{p}(y) + \int_{\Gamma} F(x,y)\dot{p}(x)\,\mathrm{d}\Gamma(x) = \int_{\Gamma} G(x,y)\dot{q}(x)\,\mathrm{d}\Gamma(x). \tag{24}$$

The discretization of the above formula allows us to evaluate $\dot{p}(y)$ as

$$\dot{p}(y) = \mathbf{g}^T(y)\dot{\mathbf{q}} - \mathbf{h}^T(y)\dot{\mathbf{p}}. \tag{25}$$

When the parameter determining the structural nodal coordinate is set as the design variable, such as the radius of the spherical shell r presented in the following numerical example, we can obtain the following formula by differentiating Eq. (22)

$$\begin{aligned}\dot{p}(y) = &\int_{\Gamma}[\dot{G}(x,y)q(x) - \dot{F}(x,y)p(x)]d\Gamma(x) + \int_{\Gamma}[G(x,y)\dot{q}(x) - F(x,y)\dot{p}(x)]d\Gamma(x)\\ &+ \int_{\Gamma}[G(x,y)q(x) - F(x,y)p(x)]d\dot{\Gamma}(x),\end{aligned} \tag{26}$$

where $\dot{G}(x,y)$ and $\dot{F}(x,y)$ can be expressed in the form of the coordinate sensitivity. For 3D acoustic wave problems, they can be expressed as

$$\dot{G}(x,y) = -\frac{e^{ikr}}{4\pi r^2}(1-ikr)\frac{\partial r}{\partial y_i}(\dot{y}_i - \dot{x}_i), \tag{27}$$

$$\dot{F}(x,y) = \frac{e^{ikr}}{4\pi r^3}\left[(3-3ikr-k^2r^2)\frac{\partial r}{\partial n(x)}\frac{\partial r}{\partial x_i} - (1-ikr)n_i(x)\right](\dot{x}_i - \dot{y}_i) - \frac{e^{ikr}}{4\pi r^2}(1-ikr)\frac{\partial r}{\partial x_i}\dot{n}_i(x), \tag{28}$$

where $\dot{x}_j$ and $\dot{y}_j$ will be evaluated when the boundary of the analyzed domain is fully parameterized with the shape design variable. $\dot{n}_l(x)$ and $d\dot{\Gamma}(x)$ can be written as

$$\dot{n}_l(x) = -\dot{x}_{j,l}n_j(x) + \dot{x}_{j,m}n_j(x)n_m(x)n_l(x), \tag{29}$$

and

$$d\dot{\Gamma}(x) = \left[\dot{x}_{l,l} - \dot{x}_{l,j}n_l(x)n_j(x)\right]d\Gamma(x), \tag{30}$$

where an index after a comma denotes the partial derivative with respect to the coordinate component and $\dot{x}_{j,m} = \partial\dot{x}_j/\partial x_m$.

Discretizing Eq. (26), we can obtain the following linear algebraic equation

$$\dot{p}(y) = \mathbf{g}_1^T(y)\mathbf{q} - \mathbf{h}_1^T(y)\mathbf{p} + \mathbf{g}^T(y)\dot{\mathbf{q}} - \mathbf{h}^T(y)\dot{\mathbf{p}}. \tag{31}$$

where $\mathbf{g}_1(y)$ and $\mathbf{h}_1(y)$ are the coefficient vectors. After substituting the solution of the vector $\mathbf{p}$, $\mathbf{q}$, $\dot{\mathbf{p}}$ and $\dot{\mathbf{q}}$ into Eq. (31) and solving Eq. (31), the sound pressure sensitivity value at any field point in the fluid domain can be obtained.

4 Element types and surface error

The approach of continuous linear and quadratic boundary elements is often applied, and the alternative of discontinuous boundary elements was investigated in previous studies [Rego-Silva (1993); Tadeu and Antonio (2000); Marburg and Schneider (2003)]. For discontinuous elements, interpolation nodes are located inside the element and the expressions of the interpolation functions are dependent on the position of the node inside the element (see Fig. 1 for quadrilaterals and Fig. 2 for triangular elements). In the two figures, 'BEmn' and 'FEmn' denote the boundary element and finite shell element with 'm' geometry nodes and 'n' interpolation nodes, respectively. For example, 'BE41' in Fig. 1 is the constant boundary element with four geometrical nodes denoting linear shape functions

being used, 'BE44' is the discontinuous linear boundary element with four geometrical nodes, 'BE91' is the constant boundary element with nine geometrical nodes denoting quadratic shape functions being used, 'BE94' is the discontinuous linear boundary element with nine geometrical nodes. The 'FE44' element is used as the isoparametric linear finite element, and the 'FE88' element as the eight-node isoparametric quadratic finite element. Although continuous boundary element is used widely, only discontinuous boundary element is used in the numerical calculations in this paper. For detailed error comparison between continuous and discontinuous boundary elements, please see paper [Marburg and Schneider (2003)]. For the constant boundary element, the interpolation node is defined at the centroid of the element. For discontinuous linear boundary element, the values of a_i and b_i decide the position of these interpolation nodes. In this paper, $a_1 = a_2 = a_3 = a_4 = 0.5$ and $b_1 = b_2 = b_3 = 0.25$ are set for simplicity [Rego-Silva (1993)]. The piecewise linear geometry approximation is implemented using elements with four or three geometrical nodes, for example BE41 in Fig. 1 and BE31 in Fig. 2. The piecewise quadratic geometry approximation is implemented using elements with nine or six nodes, for example BE91 in Fig. 1 and BE61 in Fig. 2.

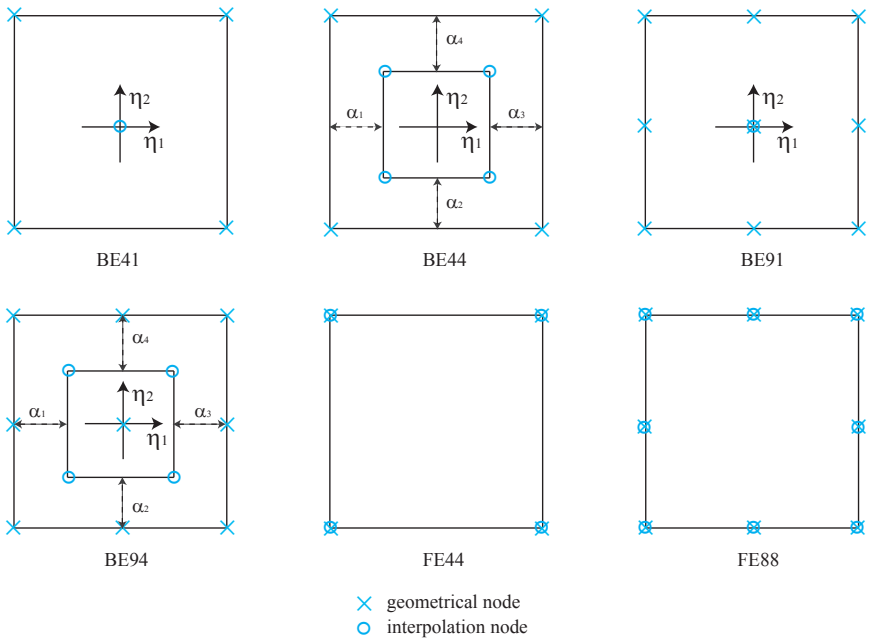

Fig. 1: Distribution of geometrical nodes and interpolation nodes in a quadrilateral element

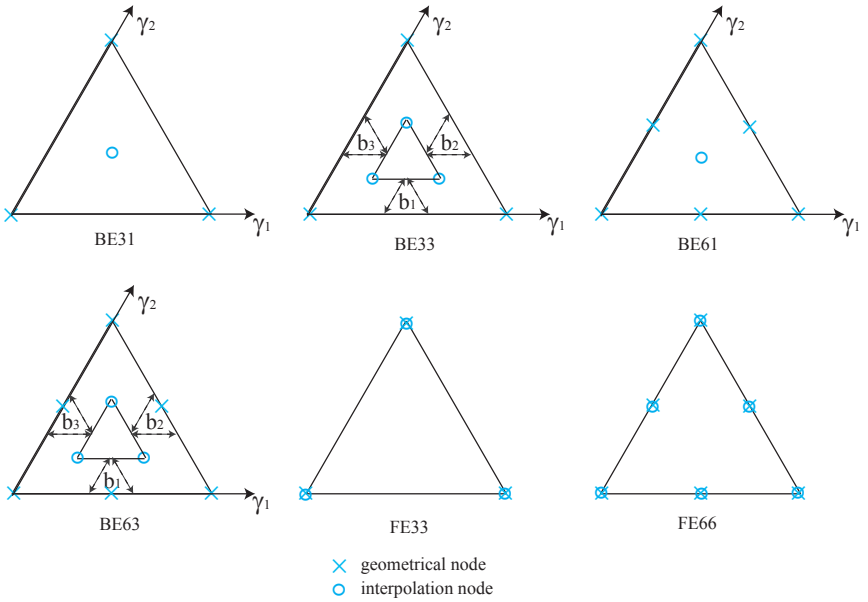

Fig. 2: Distribution of geometrical nodes and interpolation nodes in a triangular element

The solid structure is discretized using the Shell63 finite element in ANSYS for linear geometry approximation with three or four geometrical nodes, such as element FE33 and FE44, and the Shell281 finite element in ANSYS for quadratic geometry approximation with six or eight geometrical nodes, such as FE66 and FE88. The acoustic domain is discretized using constant or discontinuous linear boundary elements, such as 'BE31' and 'BE41' elements with one interpolation node for linear geometry approximation, 'BE63' with three interpolation nodes and 'BE94' elements with four interpolation nodes for quadratic geometry approximation. Every structural element is set as a boundary element, and it denotes identical mesh for the structure and fluid at the interface for the numerical solution. 'FEmn/BEmn' means that element 'FEmn' is used for the structure discretization and 'BEmn' for the acoustic domain discretization. For different 'FEmn/BEmn' element, different calculations of coupling matrix $\mathbf{C_{sf}}$ will be implemented. For the 'FE44/BE41' element, the element coupling matrix is calculated using four structural interpolation nodes and one fluid interpolation node, and the surface integration is implemented using linear geometry approximation with four nodes. For the 'FE88/BE94' element, the element coupling matrix is calculated using eight structural interpolation nodes and four fluid interpolation nodes, and the surface integration is calculated

using quadratic geometry approximation with nine geometrical nodes.

In this paper, the error function for the surface error based on the complex values is expressed as [Marburg and Schneider (2003)].

$$||e^{\Gamma}(x_i)|| = ||p_e(x_i) - p_n(x_i)||, \quad x \in \Gamma, \tag{32}$$

where p_e represents the exact solution for the sound pressure, and p_n is the numerical solution. The discrete error function is evaluated in discrete points, and the discrete surface error is determined as

$$||e^{\Gamma}||_2 = \left(\frac{1}{n} \sum_{i=1}^{n} ||e^{\Gamma}(x_i)||^2 \right)^{1/2}, \tag{33}$$

where n represents the number of nodes on the surface Γ. We then used the relative error e_2^{Γ} for the sound pressure error

$$e_2^{\Gamma} = \frac{||e^{\Gamma}||_2}{||p_e^{\Gamma}||_2}, \tag{34}$$

where $||p_e^{\Gamma}||_2$ represents the discrete Euclidean norm of the exact sound pressure and can be expressed as the following formula

$$||p_e^{\Gamma}||_2 = \left(\frac{1}{n} \sum_{i=1}^{n} ||p_e(x_i)||^2 \right)^{1/2}. \tag{35}$$

5 An example of scattering from an elastic spherical shell

In this example, we consider the acoustic scattering of a plane incident wave with a unit amplitude that travels along the positive **x** axis, as shown in Fig. 3.

The displacement $u(\theta)$ at the surface and scattered sound pressure $p(R,\theta)$ in the fluid domain, respectively, are given by [Junger and Feit (1985)]

$$u(\theta) = \frac{P_i}{k^2 r^2 \omega} \sum_{n=0}^{\infty} \frac{i^n (2n+1) P_n(cos\theta)}{Z_n + z_n} \left(\frac{\partial h_n(kr)}{\partial (kr)} \right)^{-1} \tag{36}$$

$$p(R,\theta) = -P_i \sum_{n=0}^{\infty} i^n (2n+1) P_n(cos\theta) h_n(kR) \left(\frac{\partial h_n(kr)}{\partial (kr)} \right)^{-1} \left[\left(\frac{\partial j_n(kr)}{\partial (kr)} \right) - \frac{\rho c}{k^2 r^2 (Z_n + z_n)} \left(\frac{\partial h_n(kr)}{\partial (kr)} \right)^{-1} \right] \tag{37}$$

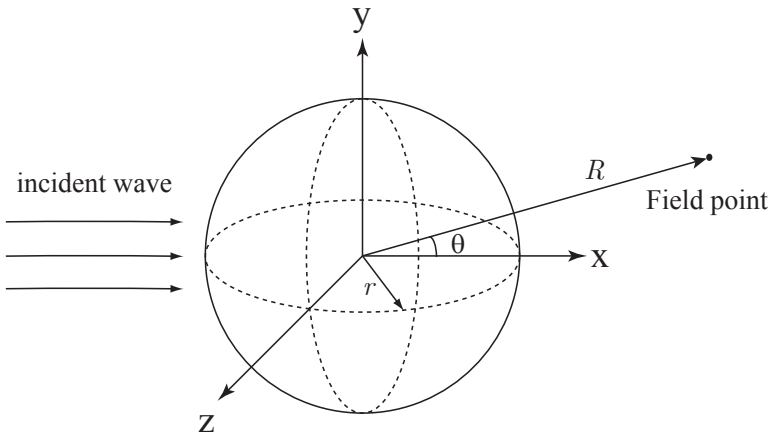

Fig. 3: Scattering from a spherical shell

where r is the radius of the spherical shell, P_n is the coefficient of the Legendre polynomials of order n. The radiation impedance z_n and modal impedance of the shell Z_n are given by

$$z_n = i\rho c h_n(kr)\left(\frac{\partial h_n(kr)}{\partial(kr)}\right)^{-1} \tag{38}$$

$$Z_n = -\frac{i\rho_s c_p}{\Omega}\frac{h}{r}\frac{\left(\Omega^2-\left(\Omega_n^{(1)}\right)^2\right)\left(\Omega^2-\left(\Omega_n^{(2)}\right)^2\right)}{\Omega^2-\lambda_n+1-\nu} \tag{39}$$

where ρ is the fluid density, c is the speed of sound in the fluid, $k=\omega/c$ is the wave number, ρ_s is the structural density, h is the thickness of the spherical shell, and h_n is the spherical Hankel functions of order n. $\lambda_n = n(n+1)$ and $c_p = \sqrt{\frac{E}{\rho_s(1-\nu^2)}}$ is the phase velocity, where E is the Young's modulus and ν is the Poisson's ratio. $\Omega = \omega r/c_p$ is the dimensionless frequency of a vibrating spherical shell. $\Omega_n^{(i)}$ is the solutions of the following characteristic frequency equation

$$\begin{aligned}&\Omega^4-\left[1+3\nu+\lambda_n-\beta^2(1-\nu-\lambda_n^2-\nu\lambda_n)\right]\Omega^2+(\lambda_n-2)(1-\nu^2)\\&\quad+\beta^2\left[\lambda_n^3-4\lambda_n^2+\lambda_n(5-\nu^2)-2(1-\nu^2)\right]=0\end{aligned} \tag{40}$$

where $\beta = h/\sqrt{12}r$.

The material data for the structure and fluid and the geometrical data are listed in Table 1. Several different meshes for the quadrilateral and triangular elements are considered. Detailed information about mesh size and number of elements is given in Table 2.

Table 1: Material and geometrical data for a submerged spherical shell

Density (water)	ρ	1000	kg/m^3
Speed of sound	c	1482	m/s
Density (steel)	ρ_s	7860	kg/m^3
Young's modulus	E	210	GPa
Poisson' ratio	v	0.3	-
Sphere radius	r	5	m
Shell thickness	h	0.05	m

Table 2: Number of quadrilateral element and triangular element for different mesh sizes.

Mesh size d (m)	Number of quadrilateral element	Number of triangular element
1.33	216	432
1.00	384	768
0.67	864	1728
0.50	1536	3072

Figures 4 and 5 present the analytical and numerical solutions for the sound pressure and displacement on the surface at 50 Hz, respectively. The FE44/BE41 element with linear shape function and the FE88/BE94 element with quadratic shape function are used to calculate the numerical solution, and a mesh size $d = 1.00$ m is used to discretize the spherical surface. The figures show that the solution obtained using the FE88/BE94 element is in agreement with the analytical solution, but the deviation of the solution with FE44/BE41 from the analytical solution is large. This result indicates that an accurate numerical solution can be obtained using a discontinuous linear boundary element with quadratic shape approximation in a moderate mesh dense.

Figure 6 presents the analytical and numerical solutions for the normalized scattered pressure on the **xy** plane at a distance $R = 100$ m from the origin point at 50 Hz. The ordinate of this figure is the normalized pressure $\bar{p} = |pR/P_i r|$, where p is the scattered pressure and P_i is the amplitude of the incident wave. The numerical solutions are computed with the FE44/BE41 and FE88/BE94 elements with $d = 1.0$ m mesh discretization. This figure shows that the solution with the FE88/BE94 element with quadratic shape approximation is in agreement with the analytical solution. However, the solution with the FE44/BE41 element with linear shape approximation has a large deviation from the analytical solution.

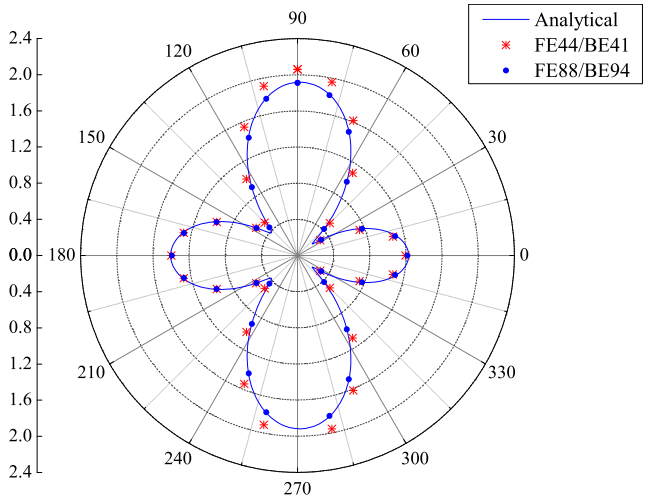

Fig. 4: Sound pressure on the surface at 50 Hz with mesh size $d = 1.00$ m

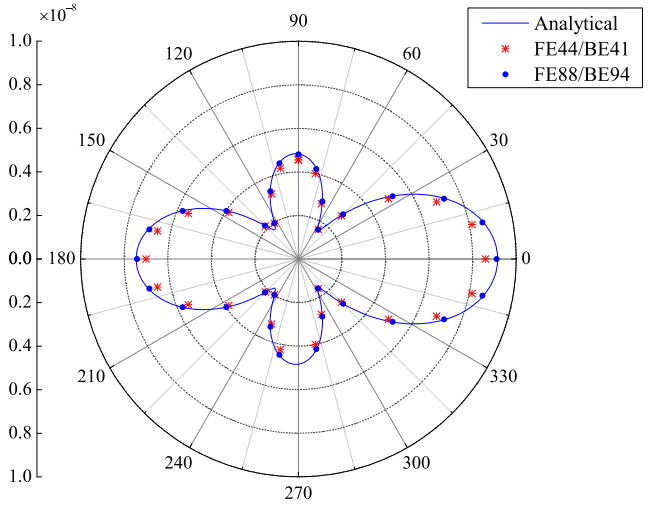

Fig. 5: Displacement on the surface at 50 Hz with mesh size $d = 1.00$ m

Figure 7 presents the analytical and the FE88/BE94 solutions for the normalized scattered pressure at a computing point $(100, 0, 0)$ in terms of frequencies. A step size of 0.002 Hz up to 100 Hz is used for evaluation of the analytical solution. The FE88/BE94 solution is evaluated in steps of 1 Hz. The mesh size $d = 0.67$ m is used for the numerical solution. The resonance frequencies are determined as 55.9 Hz, 70.5 Hz, 80.6 Hz, 88.4 Hz, and 94.8 Hz. This figure shows that there is a

good agreement between the FE88/BE94 solution and the analytical solution, and indicates the validity and correctness of the proposed algorithm in this paper.

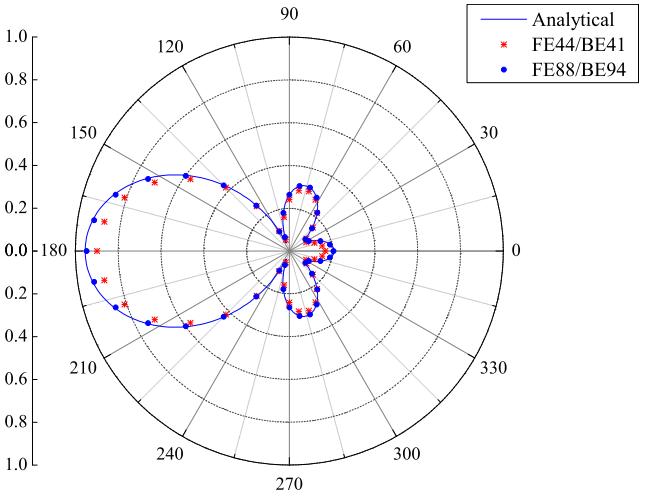

Fig. 6: Normalized scattered pressure on the xy plane at 50 Hz with mesh size $d = 1.00$ m

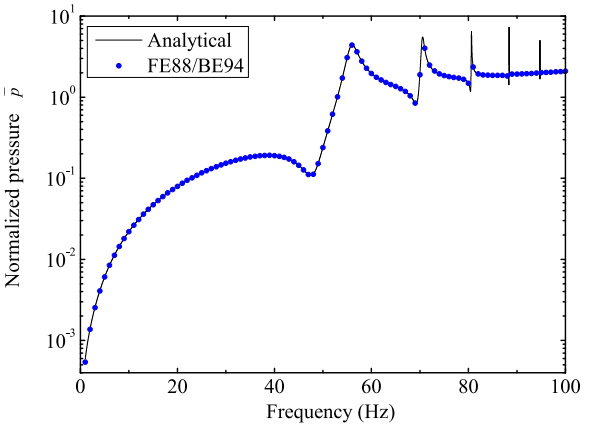

Fig. 7: Normalized scattered pressure at the computing point $(100, 0, 0)$ in terms of frequencies

Figure 8 presents the surface errors that are calculated according to Eq. (34) for the scattered pressure at a distance $R = 100$ m from the origin point with different

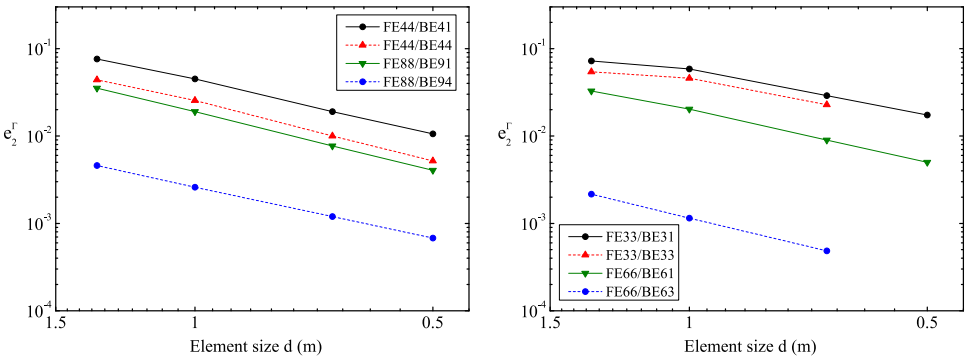

(a) Quadrilateral elements (b) Triangular elements

Fig. 8: Scattered pressure error for different elements in terms of element size at 50 Hz

elements and mesh discretization. Building and discretizing a surface are not necessary to calculate the surface error e_2^Γ because of the axisymmetry along **x** axis. Discrete points are distributed on the half circle between $\theta = 0$ and $\theta = 180$ on the **xy** plane, and the step size is set as 2 degrees and it generates 91 computing points. The figures show that the error decreases with more refined mesh discretization, and the numerical solution with higher accuracy is obtained using discontinuous linear boundary element with three or four interpolation nodes than constant boundary element. Apparently, the error obtained using elements with quadratic shape function is lower than that obtained using elements with linear shape function. In sum, the FE88/BE94 and FE66/BE63 elements perform most efficiently at the same element size. Moreover, we consider the performance of different types elements for the same degree of freedom. For the FE44/BE41 and FE88/BE91 elements, $d = 0.5$ m generates 1536 interpolation nodes; for the FE88/BE94 and FE44/BE44 elements, $d = 1.0$ m also generates 1536 interpolation nodes. For the same degree of freedom, the numerical solution with the FE44/BE41 element is 1.06E-2, 2.55E-2 with FE44/BE44, 5.44E-3 with FE88/BE91, and 2.6E-3 with FE88/BE94. The FE88/BE94 element performs mostly efficiently. The disadvantage of the linear shape functions is that a curved surface is not well-represented, which causes gaps, overlaps, and angles between elements of both meshes in the normal direction of the interaction surface. As such, more error arises when calculating the integration on the boundary surface. Moreover, the coordinate of the interpolation node obtained using linear shape approximation deviates from the analytical nodal coordinate for the curved surface, and more errors are produced. Although quadratic shape function does not provide the perfect fit for curved interfaces, the gaps and overlaps in

the normal direction of the interface are significantly reduced. On the other hand, by observing Fig. 8(b), the numerical solution for the FE66/BE63 and FE33/BE33 elements at $d = 0.5$ m cannot be obtained because of the high memory storage requirement. The linear discontinuous element generates more interpolation nodes and needs more computing time and memory storage than constant element at the same mesh size. However, the fast multipole method could be applied to overcome this problem. In the future, we will focus on this work.

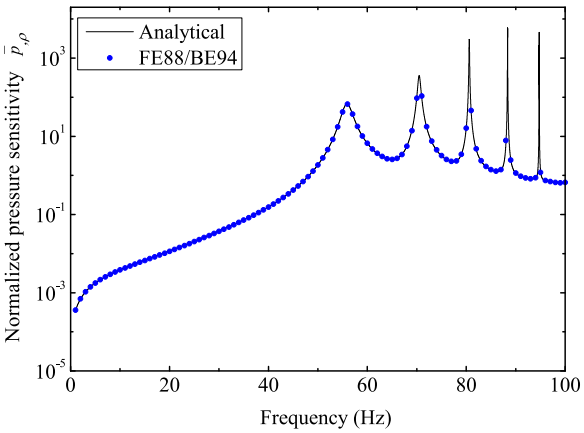

Fig. 9: The normalized far-field scattered pressure sensitivity with respect to fluid density

Figure 10 shows the analytical and the FE88/BE94 solution for the normalized scattered pressure sensitivity at a computing point $(100,0,0)$, where the design variable ϑ is chosen as the fluid density ρ, structural density ρ_s, Poisson's ratio v, Young's modulus E, thickness h and radius r, respectively. The normalized scattered pressure sensitivity $\bar{p}_{,\vartheta}$ in this paper is expressed as follows

$$\bar{p}_{,\vartheta} = \left| \frac{\partial p}{\partial \vartheta} \right| \frac{R\vartheta}{P_i r} \tag{41}$$

where p is the scattered pressure . A mesh size $d = 0.67$ m is used for the numerical solution. These figures show that the scattered pressure remains rather insensitive in the low frequency range, and the sensitivity increases in the vicinity of resonance peaks. The numerical solution is in agreement with the analytical solution. This result indicates the validity of the proposed algorithm and its correct implementation.

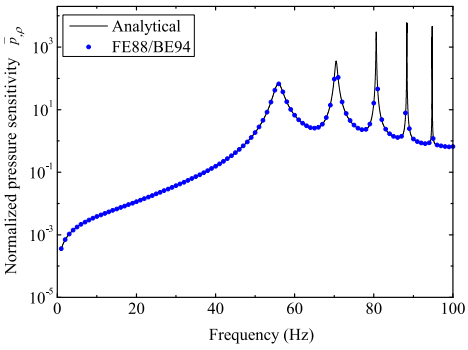

(a) Fluid density ρ

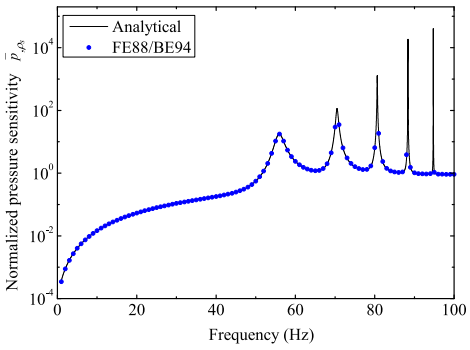

(b) Structural density ρ_s

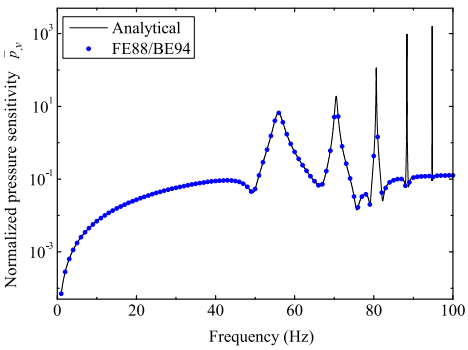

(c) Poisson's ratio v

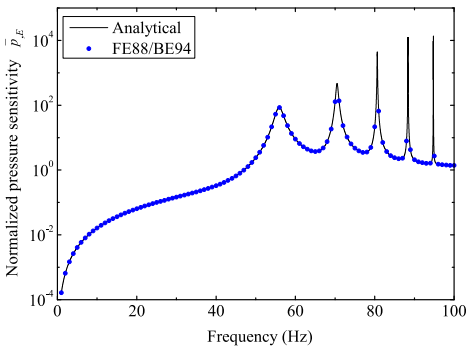

(d) Young's modulus E

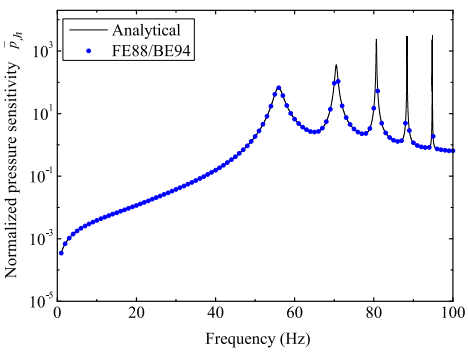

(e) Thickness h

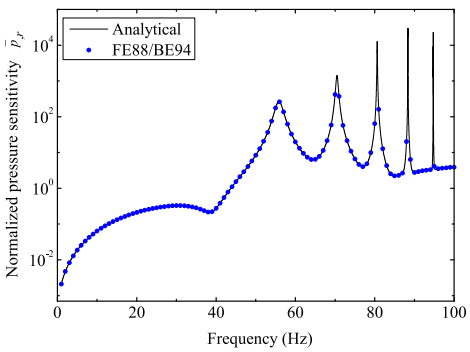

(f) Radius r

Fig. 10: The normalized scattered pressure sensitivity with respect to different design variables

6 An example of elastic spherical shell excited by an unit force

The excitation in the form of a concentrated force F applied at point A ($\theta = 0$) is taken into account, as shown in Fig. 11. The displacement $u(\theta)$ at the spheri-

cal surface and the corresponding radiated sound pressure in the fluid domain are respectively given by [Junger and Feit (1985)]

$$u(\theta) = \frac{-F}{4\pi r^2 i\omega} \sum_{n=0}^{\infty} \frac{2n+1}{Z_n + z_n} P_n(\cos\theta) \tag{42}$$

$$p(R,\theta) = \frac{i\rho cF}{4\pi r^2} \sum_{n=0}^{\infty} \frac{(2n+1)}{(Z_n + z_n)} h_n(kR) P_n(\cos\theta) \left(\frac{\partial h_n(kr)}{\partial (kr)} \right)^{-1} \tag{43}$$

where r is the radius of the spherical shell, and P_n is the coefficient of the Legendre polynomials of order n. The radiation impedance z_n and modal impedance of the shell Z_n are defined in Eq. (38) and (39). The material data for the structure and fluid and the geometrical data are the same as those in the example of the scattered sphere, and are listed in Table 1.

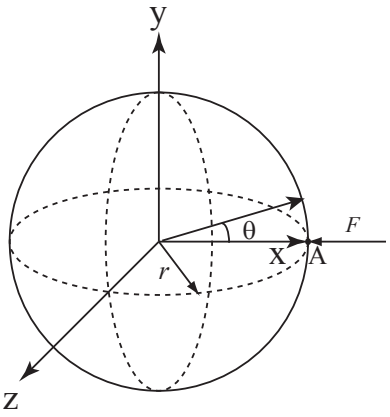

Fig. 11: Spherical shell excited by a single force at point A

Figures 12 and 13 present the analytical and numerical solutions for the amplitudes of the radiated sound pressure and displacement, respectively, on the surface at 50 Hz. The numerical solutions are computed with the FE44/BE41 and FE88/BE94 elements with $d = 1.0$ m mesh discretization. The figures show that the numerical solution obtained using the FE88/BE94 element with quadratic shape approximation is in agreement with the analytical solution, but the deviation of the solution with the FE44/BE41 element from the analytical solution is large. This result denotes that a more accurate solution can be obtained using discontinuous linear boundary element with quadratic shape approximation.

Figure 14 presents the analytical and numerical solutions for the amplitude of the radiated sound pressure at the points distributed on the **xy** plane at a distance

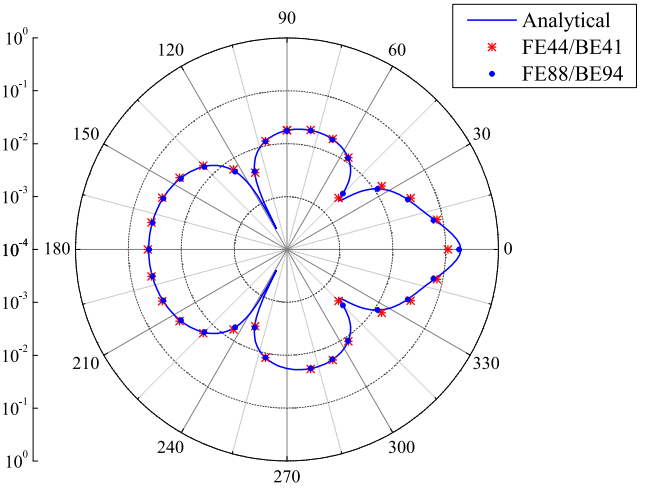

Fig. 12: Sound pressure on the surface at 50 Hz with mesh size $d = 1.0$ m

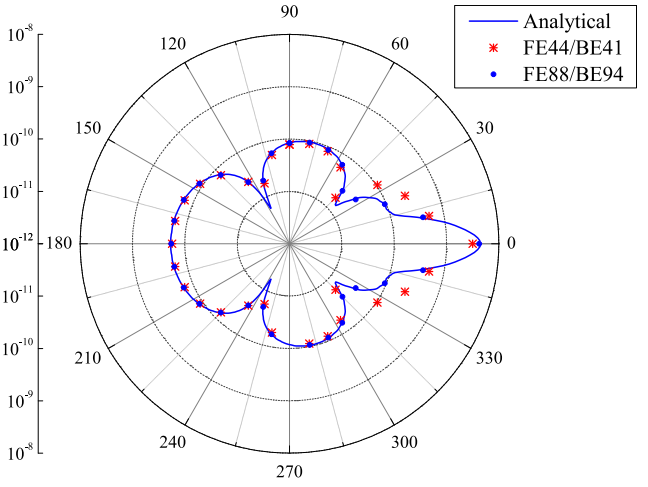

Fig. 13: Displacement on the surface at 50 Hz $d = 1.0$ m

$R = 100$ m from the origin point at 50 Hz. This figure shows that accurate numerical solution can be obtained using the FE88/BE94 element with quadratic shape function. Figure 15 presents the analytical and the FE88/BE94 solutions for the amplitude of the radiated sound pressure at a computing point $(100, 0, 0)$ in terms of frequencies. A step size of 0.002 Hz up to 100 Hz is used for evaluation of the analytical solution, whereas the FE88/BE94 solution is evaluated in steps of 1 Hz. A mesh size $d = 0.67$ m is used for the numerical solution. This figure shows that

there is a good agreement between the FE88/BE94 solution and the analytical solution and indicates the validity and correctness of the proposed algorithm in this paper.

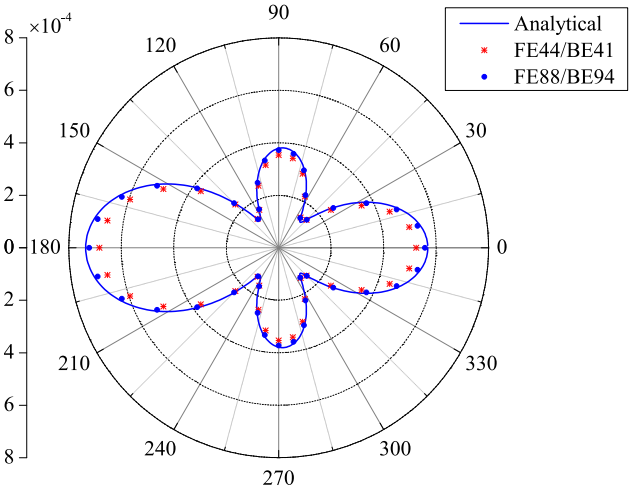

Fig. 14: Radiated pressure on the **xy** plane at a distance $R = 100m$ at 50 Hz

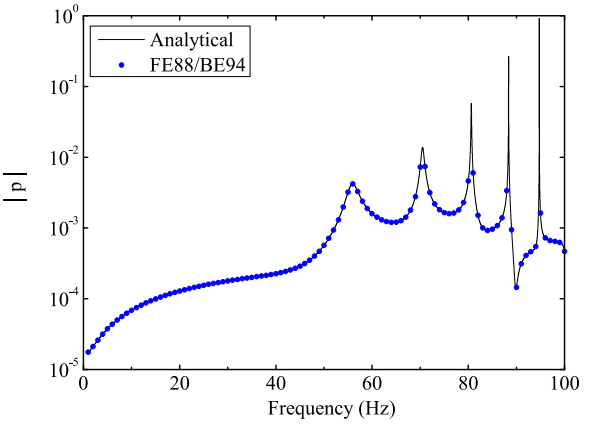

Fig. 15: Radiated sound pressure at point $(100, 0, 0)$ in terms of frequencies.

Figure 16 presents the surface errors that are calculated according to Eq. (34) for the radiated sound pressure at a distance $R = 100$ m from the origin point with different elements and mesh discretization. Building and discretizing a surface for calculating the surface error e_2^{Γ} are not necessary because of the axisymmetry along x axis.

Discrete points are distributed on the half circle between $\theta = 0$ and $\theta = 180$ on the xy plane, and the step size is set as 2 degrees and it generates 91 computing points. The figures show that the error decreases with a more refined mesh discretization, and the numerical solution with a higher accuracy is obtained using discontinuous linear boundary element with three or four interpolation nodes than constant boundary element. The error obtained using elements with quadratic shape function is lower than that obtained using elements with linear shape function. In sum, the FE88/BE94 and FE66/BE63 elements perform most efficiently at the same element size. We then consider the performance of different types elements for the same degree of freedom. For the FE44/BE41 and FE88/BE91 elements, $d = 0.5$ m generates 1536 interpolation nodes; for the FE88/BE94 and FE44/BE44 elements, $d = 1.0$ m also generates 1536 interpolation nodes. For the same degree of freedom, the numerical solution with the FE44/BE41 element is 1.83E-2, 3.12E-2 with FE44/BE44, 1.32E-2 with FE88/BE91, and 3.33E-3 with FE88/BE94. Thus, the FE88/BE94 element performs mostly efficiently.

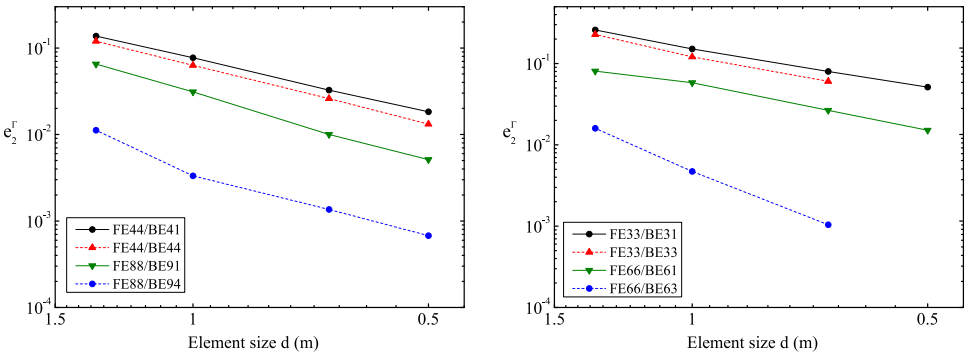

(a) Quadrilateral elements (b) Triangular elements

Fig. 16: Radiated sound pressure error for different elements in terms of element size at 50 Hz

Figure 17 shows the analytical and the FE88/BE94 solution for the amplitude of the radiated sound pressure sensitivity at a computing point $(100,0,0)$, where the design variable ϑ is set as the fluid density ρ, structural density ρ_s, Poisson's ratio v, Young's modulus E, thickness h and radius r, respectively. A mesh size $d = 0.67$ m is used for the numerical solution. These figures show that the radiated pressure remains rather insensitive in the low frequency range, and the sensitivity goes up in the vicinity of resonance peaks. The numerical solution agrees with the analytical solution which indicates the validity of the proposed algorithm and its correct implementation.

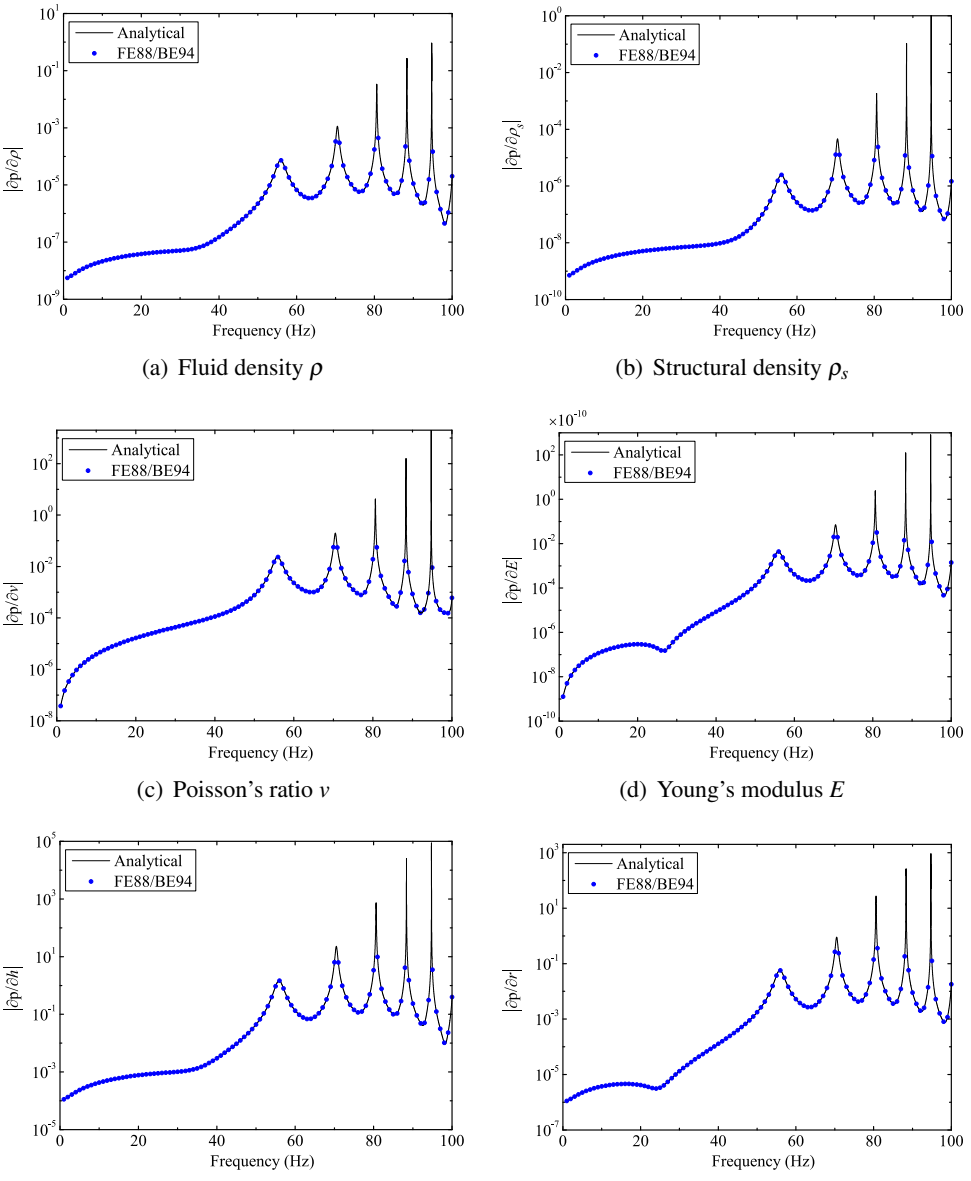

(a) Fluid density ρ (b) Structural density ρ_s

(c) Poisson's ratio v (d) Young's modulus E

(e) Thickness h (f) Radius r

Fig. 17: The radiated sound pressure sensitivity with respect to different design variables

7 Conclusions

A coupling algorithm based on FEM and BEM is presented for the simulation of fluid-structure interaction and structural acoustic sensitivity analysis using the di-

rect differentiation method, where the design variable is set as the fluid density, structural density, Poisson's ratio, Young's modulus, structural thickness and radius, respectively. For different design variables, the different formulations are presented for the calculation of the derivatives to the sound pressure. Numerical examples are presented to demonstrate the validity of the proposed algorithm. Different types elements are used for the numerical solution, and the performance of different types of FE/BE element is presented and compared. The discontinuous linear boundary elements with quadratic shape approximation perform more efficiently than the constant boundary elements with linear shape approximation.

The algorithm presented in this paper makes it possible to predict the effects of different design variables on the radiation and scattered sound field numerically. Future work will include applying the structural-acoustic design sensitivity analysis to optimize and extending the method to practical engineering problems.

Acknowledgement: Financial supports from the China Scholarship Council (CSC), National Natural Science Foundation of China (NSFC) under Grant no. 11172291, Research Fund for the Doctoral Program of Higher Education of China under Grand no. 20133402110036, and USTC under Grant no. WK2090000007 are acknowledged.

References

Atkinson, K. (1997): *The Numerical Solution of Integral Equations of the Second Kind* . Cambridge University Press.

Brunner, D.; Junge, M.; Gaul, L. (2009): A comparison of FE-BE coupling schemes for large-scale problems with fluid-structure interaction . *International Journal for Numerical Methods in Engineering*, vol. 77, pp. 664–688.

Burton, A.; Miller, G. (1971): The application of integral equation methods to the numerical solution of some exterior boundary-value problems . *Proc. Roy. Soc. Lond. A.*, vol. 323, pp. 201–210.

Chen, L.; Chen, H.; Zheng, C. (2013): FEM/wideband FMBEM coupling for fluid-structure interaction problem and 2D acoustic design sensitivity analysis . *CMES: Computer Modeling in Engineering & Sciences*, vol. 94, pp. 459–484.

Chen, L.; Zheng, C.; Chen, H. (2013): A wideband FMBEM for 2D acoustic design sensitivity analysis based on direct differentiation method . *Computational Mechanics*, vol. 52, pp. 631–648.

Chen, L.; Zheng, C.; Chen, H. (2014): FEM/wideband FMBEM coupling for structural-acoustic design sensitivity analysis . *Computer Methods in Applied Mechanics and Engineering*, vol. 276, pp. 1–19.

Chen, Z.; Hofstetter, G.; Mang, H. (1998): A Galerkin-type BE-FE formulation for elasto-acoustic coupling. *Computer Methods in Applied Mechanics and Engineering*, vol. 152, pp. 147–155.

Chien, C.; Rajiyah, H.; Atluri, S. (1990): An Effective Method for Solving the Hyper-Singular Integral Equations in 3-D Acoustics. *Journal of the Acoustical Society of America*, vol. 88, pp. 918–937.

Choi, K.; Shim, I.; Wang, S. (1997): Design sensitivity analysis of structure-induced noise and vibration. *Journal of Vibration and Acoustics*, vol. 119, pp. 173–179.

Everstine, G.; Henderson, F. (1990): Coupled finite element/boundary element approach for fluid-structure interaction. *Journal of the Acoustic Society of America*, vol. 87, pp. 1938–1947.

Fischer, M.; Gaul, L. (2005): Fast BEM-FEM mortar coupling for acoustic-structure interaction . *International Journal for Numerical Methods in Engineering*, vol. 62, pp. 1677–1690.

Fritze, D.; Marburg, S.; Hardtke, H. (2005): FEM-BEM-coupling and structural-acoustic sensitivity analysis for shell geometries. *Computers and Structures*, vol. 82, pp. 143–154.

Hambric, S. A. (1996): Sensitivity calculations for broad-band acoustic radiated noise design optimization problems. *Journal of Vibration and Acoustics*, vol. 118, pp. 529–532.

Han, Z.; Atluri, S. (2002): SGBEM (for cracked local subdomain)-FEM (for uncracked global structure) alternating method for analyzing 3D surface cracks and their fatigue-growth. *CMES: Computer Modeling in Engineering & Sciences*, vol. 3, pp. 699–716.

Junge, M.; Brunner, D.; Gaul, L. (2011): Solution of FE-BE coupled eigenvalue problems for the prediction of the vibro-acoustic behavior of ship-like structures . *International Journal for Numerical Methods in Engineering*, vol. 87, pp. 664–676.

Junger, M. C.; Feit, D. (1985): *Structures and Their Interaction*. MIT Press.

Lamancusa, J. S. (1993): Numerical optimization techniques for structural-acoustic design of rectangular panels. *Composite Structures*, vol. 48, pp. 661–675.

Lie, S.; Yu, G.; Zhao, Z. (2001): Coupling of BEM/FEM for time domain structural-acoustic interaction problem. *CMES: Computer Modeling in Engineering & Sciences*, vol. 2, pp. 171–182.

Marburg, S. (2002): Developments in structural-acoustic optimization for passive noise control. *Archives of Computational Methods in Engineering*, vol. 27, pp. 291–370.

Marburg, S.; Schneider, S. (2003): Influence of element types on numeric error for acoustic boundary elements . *Journal of Computational Acoustics*, vol. 11, pp. 363–386.

Matsumoto, T.; Yamada, T.; Takahashi, T.; Zheng, C.; Harada, S. (2011): Acoustic design shape and topology sensitivity formulations based on adjoint method and BEM. *CMES: Computer Modeling in Engineering & Sciences*, vol. 78, no. 2, pp. 77–94.

Merz, S.; Kinns, R.; Kessissoglou, N. (2009): Structural and acoustic responses of a submarine hull due to propeller forces. *Jounal of Sound and Vibration*, vol. 325, pp. 266–286.

Okada, H.; Fukui, Y.; Kumazawa, N. (2004): Homogenization analysis for particulate composite materials using the boundary element method. *CMES: Computer Modeling in Engineering & Sciences*, vol. 5, pp. 135–150.

Peters, H.; Marburg, S.; Kessissoglou, N. (2012): Structural-acoustic coupling on non-conforming meshes with quadratic shape functions . *International Journal for Numerical Methods in Engineering*, vol. 91, pp. 27–38.

Qian, L.; Batra, R.; Chen, L. (2003): Elastostatic deformations of a thick plate by using a higher-order shear and normal deformable plate theory and two meshless local Petrov-Galerkin (MLPG) methods. *CMES: Computer Modeling in Engineering & Sciences*, vol. 4, pp. 161–175.

Qian, Z.; Han, Z.; Atluri, S. (2004): Directly derived non-hyper-singular boundary integral equations for acoustic problems, and their solution through Petrov-Calerkin schemes. *CMES: Computer Modeling in Engineering & Sciences*, vol. 5, pp. 541–562.

Qian, Z.; Han, Z.; Atluri, S. (2013): A Fast Regularized Boundary Integral Method for Practical Acoustic Problems. *CMES: Computer Modeling in Engineering & Sciences*, vol. 91, pp. 463–484.

Qian, Z.; Han, Z.; Ufimtsev, P.; Atluri, S. (2004): Non-hyper-singular boundary integral equations for acoustic problems, implemented by the collocation-based boundary element method. *CMES: Computer Modeling in Engineering & Sciences*, vol. 6, pp. 133–144.

Rego-Silva, J. (1993): *Acoustic and Elastic Wave Scattering Using Boundary Elements*. Southampton, Boston: Computational Mechanics Publications.

Saad, Y. (1996): Iterative Methods for Sparse Linear Systems.

Schneider, S. (2008): FE/FMBE coupling to model fluid-structure interaction . *International Journal for Numerical Methods in Engineering*, vol. 76, pp. 2137–2156.

Tadeu, A.; Antonio, J. (2000): Use of constant, linear and quadratic boundary elements in 3d wave diffraction analysis . *Eng. Anal. Boundary Elem.*, vol. 24, pp. 131–144.

Wang, S. (1999): Design sensitivity analysis of noise, vibration and harshness of vehicle body structure. *Mechanics of Structures and Machines*, vol. 27, pp. 317–336.

Zheng, C.; Chen, H.; Matsumoto, T.; Takahashi, T. (2011): Three dimensional acoustic shape sensitivity analysis by means of adjoint variable method and fast multipole boundary element approach. *CMES: Computer Modeling in Engineering & Sciences*, vol. 79, no. 1, pp. 1–30.

Zheng, C.; Matsumoto, T.; Takahashi, T.; Chen, H. (2012): A wideband fast multipole boundary element method for three dimensional acoustic shape sensitivity analysis based on direct differentiation method . *Eng. Anal. Boundary Elem.*, vol. 36, pp. 361–371.